

Electronic Properties of Multilayer Graphene

Hongki Min

Center for Nanoscale Science and Technology, National Institute of Standards and Technology, Gaithersburg, Maryland 20899-6202, USA; Maryland NanoCenter, University of Maryland, College Park, Maryland 20742, USA; Current address: Department of Physics and Astronomy, Seoul National University, Seoul 151-747, Korea. hmin@snu.ac.kr

Abstract. In this chapter, we study the electronic structure of arbitrarily stacked multilayer graphene in the absence or presence of magnetic field. The energy band structure and the Landau level spectrum are obtained using a π -orbital continuum model with nearest-neighbor intralayer and interlayer tunneling terms. Using degenerate state perturbation theory, we analyze the low-energy effective theory and show that the low-energy electronic structure of arbitrarily stacked graphene multilayers consists of chiral pseudospin doublets with a conserved chirality sum. We discuss the implications of this for the quantum Hall effect, optical conductivity and electrical conductivity.

11.1 Introduction

The recent explosion [1–6] of research on the electronic properties of single layer and stacked multilayer graphene sheets has been driven by advances in material preparation methods [7,8], by the unusual [9–11] electronic properties of these materials including unusual quantum Hall effects [12,13], and by hopes that these elegantly tunable systems might be useful electronic materials.

Electronic properties of multilayer graphene strongly depend on the stacking sequence. Periodically stacked multilayer graphene [14–19] and arbitrarily stacked multilayer graphene [20,21] have been studied theoretically, demonstrating that the low-energy band structure of graphene multilayer consists of a set of independent pseudospin doublets. It was shown that energy gap can be induced by a perpendicular external electric field in ABC-stacked multilayer graphene [22,23]. Furthermore, in ABC stacking electron-electron interactions play more important role than other stacking sequences due to the appearance of relatively flat bands near the Fermi level [23]. Optical properties of multilayer graphene using absorption spectroscopy have been studied experimentally [24] and theoretically [25–28] showing characteristic peak positions in optical conductivity depending on stacking sequences. Transport properties of multilayer graphene have been studied theoretically within the coher-

ent potential approximation for averaged local impurities [29–31] and using Boltzmann transport theory [32, 33]. (See Chapter 12 for transport theory in graphene.)

In this chapter, we describe the electronic structure of arbitrarily stacked multilayer graphene and analyze its low-energy spectrum. (Here we are not considering graphene sheets with rotational stacking faults, which typically appear in epitaxial graphene grown on carbon-face SiC substrate and behave as a collection of decoupled monolayer graphene [34–36].) Interestingly, the low-energy effective theory of multilayer graphene is always described by a set of chiral pseudospin doublets with a conserved chirality sum. We discuss implications of this finding for the quantum Hall effect, optical conductivity and electrical conductivity in multilayer graphene. (See Chapter 8 for electronic properties of monolayer and bilayer graphene.)

11.1.1 Stacking arrangements

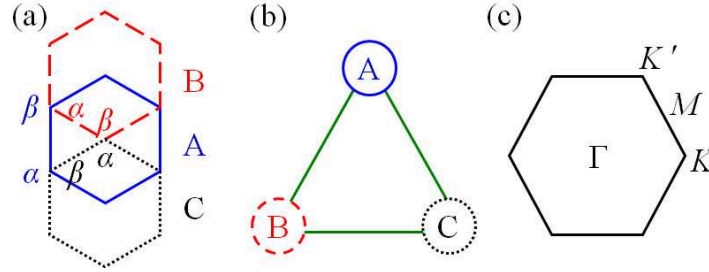


Fig. 11.1. (a) Three distinct stacking arrangements A, B and C in multilayer graphene and representative sublattices α and β in the A, B, and C layers. (b) The stacking triangle where each added layer cycles around. (c) Brillouin zone of the honeycomb lattice.

In multilayer graphene, there are three distinct stacking arrangements, labeled A, B and C, classified by the relative position in two-dimensional (2D) plane, and in each plane the honeycomb lattice of a single sheet has two triangular sublattices, labeled by α and β , as illustrated in Fig. 11.1(a). (Here we use α and β for sublattices instead of A and B to avoid any confusion with stacking arrangements, A, B and C.) Different stacking types are obtained by displacing sublattices along the honeycomb edges or by rotating by $\pm 60^\circ$ about a carbon atom on one of the two sublattices. Special stacking sequences are generated by repeated AB, ABC and AA stacking, and are called Bernal, rhombohedral and hexagonal stacking, respectively.

Each added layer cycles around the stacking triangle in either the right-handed or the left-handed sense, or stays at the same position in the triangle,

as seen in Fig. 11.1(b). For example, Bernal (AB) stacking corresponds to moving with a reversal in direction at every step, and rhombohedral (ABC) stacking corresponds to moving with no reversals in direction, while hexagonal (AA) stacking corresponds to not moving around the triangle at all. As discussed later, the cyclic motion in the stacking triangle is closely related to the chirality of multilayer graphene.

11.1.2 π -orbital continuum model

In graphene, p_z orbitals form low-energy bands near the Fermi energy while sp^2 -hybridized s , p_x and p_y orbitals form high-energy bands. They are also called π -orbitals and σ -orbitals, respectively, from the symmetry of the orbital shape. The π -orbital continuum model for the N -layer graphene Hamiltonian describes energy bands near the hexagonal corners of the Brillouin zone, the K and K' points (Fig. 11.1(c)):

$$\mathcal{H} = \sum_{\mathbf{p}} \Psi_{\mathbf{p}}^\dagger H(\mathbf{p}) \Psi_{\mathbf{p}}, \quad (11.1)$$

where $\Psi_{\mathbf{p}} = (c_{1,\alpha,\mathbf{p}}, c_{1,\beta,\mathbf{p}}, \dots, c_{N,\alpha,\mathbf{p}}, c_{N,\beta,\mathbf{p}})$ and $c_{l,\mu,\mathbf{p}}$ is an electron annihilation operator for layer $l = 1, \dots, N$, sublattice $\mu = \alpha, \beta$ and 2D momentum \mathbf{p} measured from the K or K' point. The K and K' points are often called *valleys*.

The simplest model for a multilayer graphene system allows only nearest-neighbor intralayer hopping t and the nearest-neighbor interlayer hopping t_\perp . The monolayer graphene quasiparticle velocity $v \approx 10^6$ m/s is related with t by $\frac{\hbar v}{a} = \frac{\sqrt{3}}{2}t$, where $a = 0.246$ nm is a lattice constant of monolayer graphene. (In this chapter, for simplicity, $t \approx 3$ eV and $t_\perp \approx 0.3$ eV will be used in numerical calculations. See Chapter 8 for discussion of the values of hopping parameters and other neglected remote hopping terms. See also Ref. [16].) Although this minimal model is not fully realistic, some aspects of the electronic structure can be easily understood by fully analyzing the properties of this model. We describe limitations of the minimal model later.

11.2 Energy band structure

11.2.1 Preliminaries

Before analyzing the energy spectrum of multilayer graphene, let us consider the Hamiltonian of a one-band tight-binding model for a one-dimensional (1D) chain of length N with nearest-neighbor hopping parameter t_\perp , as illustrated in Fig. 11.2:

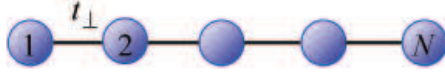


Fig. 11.2. Chain of length N with nearest-neighbor hopping parameter t_{\perp} .

$$H = \begin{pmatrix} 0 & t_{\perp} & 0 & 0 \\ t_{\perp} & 0 & t_{\perp} & 0 \\ 0 & t_{\perp} & 0 & t_{\perp} & \cdots \\ 0 & 0 & t_{\perp} & 0 \\ & & \cdots & \end{pmatrix}. \quad (11.2)$$

This Hamiltonian is important for analyzing the role of interlayer hopping as explained below.

Let $\mathbf{a} = (a_1, \dots, a_N)$ be an eigenvector with an eigenvalue ε . Then the eigenvalue problem reduces to the following difference equation

$$\varepsilon a_n = t_{\perp} (a_{n-1} + a_{n+1}), \quad (11.3)$$

with the boundary condition $a_0 = a_{N+1} = 0$. Assuming $a_n \sim e^{in\theta}$, it can be shown that [37]

$$\begin{aligned} \varepsilon_r &= 2 t_{\perp} \cos \theta_r, \\ \mathbf{a}_r &= \sqrt{\frac{2}{N+1}} (\sin \theta_r, \sin 2\theta_r, \dots, \sin N\theta_r), \end{aligned} \quad (11.4)$$

where $r = 1, 2, \dots, N$ is the chain eigenvalue index and $\theta_r = r\pi/(N+1)$. Note that odd N chains have a zero-energy eigenstate at $r = (N+1)/2$ with an eigenvector that has nonzero constant amplitude on every other positions alternating in sign.

11.2.2 Monolayer graphene

First, let's briefly review the effective Hamiltonian of monolayer graphene. (See Chapter 8 for detailed discussion of the effective Hamiltonian of monolayer and bilayer graphene.) In the absence of spin-orbit interactions, π -orbitals are decoupled from other orbitals forming low-energy bands near the Fermi energy. The Hamiltonian for the decoupled π -orbitals is given by [38]

$$H(\mathbf{k}) = \begin{pmatrix} 0 & (-t)f(\mathbf{k}) \\ (-t)f^*(\mathbf{k}) & 0 \end{pmatrix}, \quad (11.5)$$

where t is the (positive) nearest neighbor intralayer hopping parameter and

$$f(\mathbf{k}) = e^{i\frac{k_y a}{\sqrt{3}}} + 2 \cos\left(\frac{k_x a}{2}\right) e^{-i\frac{k_y a}{2\sqrt{3}}}. \quad (11.6)$$

Here we chose a coordinate system in which the honeycomb Bravais lattice has primitive vectors, $\mathbf{a}_1 = a(1, 0)$ and $\mathbf{a}_2 = a\left(\frac{1}{2}, \frac{\sqrt{3}}{2}\right)$.

At the K and K' points, $f(\mathbf{k})$ becomes zero. Among the equivalent K or K' points, we can choose $K = (\frac{4\pi}{3a}, 0)$ and $K' = -K$ for simplicity. If we expand $f(\mathbf{k})$ around the K point, the effective Hamiltonian near the K point can be obtained as

$$H^K(\mathbf{q}) = \begin{pmatrix} 0 & \hbar v(q_x - iq_y) \\ \hbar v(q_x + iq_y) & 0 \end{pmatrix}, \quad (11.7)$$

where $\frac{\hbar v}{a} = \frac{\sqrt{3}}{2}t$ and \mathbf{q} is a wavevector measured from the K point. Similarly, if we expand $f(\mathbf{k})$ around the K' point, the effective Hamiltonian near the K' point can be obtained as

$$H^{K'}(\mathbf{q}) = \begin{pmatrix} 0 & -\hbar v(q_x + iq_y) \\ -\hbar v(q_x - iq_y) & 0 \end{pmatrix}, \quad (11.8)$$

where \mathbf{q} is measured from the K' point.

In a compact form, Eqs. 11.7 and 11.8 can be combined as

$$H^{K/K'}(\mathbf{q}) = \hbar v(\tau_z q_x \sigma_x + q_y \sigma_y), \quad (11.9)$$

where σ_α are Pauli matrices describing the sublattice degrees of freedom, $\tau_z = 1$ for the K point and $\tau_z = -1$ for the K' point, respectively. From now on, for multilayer graphene we will only consider the Hamiltonian near the K point. The Hamiltonian near the K' point can easily be obtained using Eq. 11.8.

11.2.3 AA stacking

In the case of AA stacking, there is vertical hopping between $\alpha - \alpha$ sites and between $\beta - \beta$ sites. Thus, the Hamiltonian at K in the $(\alpha_1, \beta_1, \alpha_2, \beta_2, \dots)$ basis is given by

$$H_{AA}(\mathbf{p}) = \begin{pmatrix} 0 & v\pi^\dagger & t_\perp & 0 & 0 & 0 \\ v\pi & 0 & 0 & t_\perp & 0 & 0 \\ t_\perp & 0 & 0 & v\pi^\dagger & t_\perp & 0 \\ 0 & t_\perp & v\pi & 0 & 0 & t_\perp \cdots \\ 0 & 0 & t_\perp & 0 & 0 & v\pi^\dagger \\ 0 & 0 & 0 & t_\perp & v\pi & 0 \\ & & & \dots & & \end{pmatrix}, \quad (11.10)$$

where $\mathbf{p} = \hbar\mathbf{k}$, \mathbf{k} is a wavevector measured from the K point and $\pi = p_x + ip_y$.

For an eigenvector $(a_1, b_1, \dots, a_N, b_N)$ with an eigenvalue ε and fixed 2D momentum, the difference equations in this case are

$$\begin{aligned}\varepsilon a_n &= t_\perp(a_{n-1} + a_{n+1}) + v\pi^\dagger b_n, \\ \varepsilon b_n &= t_\perp(b_{n-1} + b_{n+1}) + v\pi a_n,\end{aligned}\quad (11.11)$$

with the boundary condition $a_0 = a_{N+1} = b_0 = b_{N+1} = 0$.

Let $c_n \equiv a_n + b_n e^{-i\phi}$ and $d_n \equiv a_n - b_n e^{-i\phi}$ where $\phi = \tan^{-1}(p_y/p_x)$. Then

$$\begin{aligned}(\varepsilon - v|\mathbf{p}|)c_n &= t_\perp(c_{n-1} + c_{n+1}), \\ (\varepsilon + v|\mathbf{p}|)d_n &= t_\perp(d_{n-1} + d_{n+1}),\end{aligned}\quad (11.12)$$

with the same boundary condition $c_0 = c_{N+1} = d_0 = d_{N+1} = 0$. Thus, the electronic structure of AA-stacked N -layer graphene can be thought of as consisting of separate 1D chains for each wavevector in the 2D honeycomb lattice Brillouin zone. Then the energy spectrum is given by

$$\varepsilon_{r,\mathbf{p}}^\pm = \pm v|\mathbf{p}| + 2t_\perp \cos\left(\frac{r\pi}{N+1}\right), \quad (11.13)$$

where $r = 1, 2, \dots, N$. Note that for odd N , the $r = (N+1)/2$ mode provides two zero-energy states at $\mathbf{p} = 0$ per spin and valley.

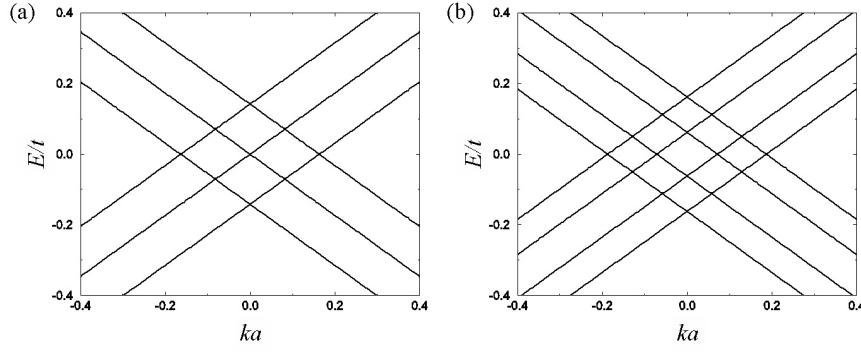


Fig. 11.3. Energy band structure near the K point for AA-stacked (a) trilayer and (b) tetralayer graphene with nearest-neighbor intralayer hopping $t = 3$ eV and nearest-neighbor interlayer hopping $t_\perp = 0.1t$. k is a wavevector measured from the K point and a is a lattice constant of graphene.

Fig. 11.3 shows the band structure of AA-stacked trilayer and tetralayer graphene near the K point. Because of the hybridization between $\alpha - \alpha$ and $\beta - \beta$ sublattices in each layer, additional zero-energy states can occur at momenta that are remote from the K and K' points.

11.2.4 AB stacking

In the case of AB stacking, there is vertical hopping between $\beta_1 - \alpha_2 - \beta_3 - \alpha_4 - \dots$ sites from the bottom layer. Thus, the Hamiltonian at K in the

$(\alpha_1, \beta_1, \alpha_2, \beta_2, \dots)$ basis has the following form,

$$H_{AB}(\mathbf{p}) = \begin{pmatrix} 0 & v\pi^\dagger & 0 & 0 & 0 & 0 \\ v\pi & 0 & t_\perp & 0 & 0 & 0 \\ 0 & t_\perp & 0 & v\pi^\dagger & 0 & t_\perp \\ 0 & 0 & v\pi & 0 & 0 & 0 & \dots \\ 0 & 0 & 0 & 0 & 0 & v\pi^\dagger \\ 0 & 0 & t_\perp & 0 & v\pi & 0 \\ & & & \dots & & \end{pmatrix}. \quad (11.14)$$

The subtle difference in this Hamiltonian compared to the AA case changes the electronic structure in a qualitative way. To obtain the energy spectrum of AB-stacked N -layer graphene, let us consider corresponding difference equations [15]:

$$\begin{aligned} \varepsilon a_{2n-1} &= (v\pi^\dagger) b_{2n-1}, \\ \varepsilon b_{2n-1} &= t_\perp (a_{2n-2} + a_{2n}) + (v\pi) a_{2n-1}, \\ \varepsilon a_{2n} &= t_\perp (b_{2n-1} + b_{2n+1}) + (v\pi^\dagger) b_{2n}, \\ \varepsilon b_{2n} &= (v\pi) a_{2n}, \end{aligned} \quad (11.15)$$

with the boundary condition $a_0 = a_{N+1} = b_0 = b_{N+1} = 0$.

Letting $c_{2n-1} \equiv b_{2n-1}$ and $c_{2n} \equiv a_{2n}$, the difference equations reduce to

$$(\varepsilon - v^2 |\mathbf{p}|^2 / \varepsilon) c_n = t_\perp (c_{n-1} + c_{n+1}), \quad (11.16)$$

with the boundary condition $c_0 = c_{N+1} = 0$. Then the energy spectrum is given by

$$\varepsilon - v^2 |\mathbf{p}|^2 / \varepsilon = 2t_\perp \cos \left(\frac{r\pi}{N+1} \right), \quad (11.17)$$

where $r = 1, 2, \dots, N$. Thus

$$\varepsilon_{r,\mathbf{p}}^\pm = t_\perp \cos \left(\frac{r\pi}{N+1} \right) \pm \sqrt{v^2 |\mathbf{p}|^2 + t_\perp^2 \cos^2 \left(\frac{r\pi}{N+1} \right)}. \quad (11.18)$$

Note that the relativistic energy spectrum for a particle with the momentum \mathbf{p} and mass m is given by

$$\varepsilon_{\mathbf{p}} = \sqrt{|\mathbf{p}|^2 c^2 + m^2 c^4}, \quad (11.19)$$

where c is the velocity of light. Thus the effective mass can be identified as $m_r v^2 = \left| t_\perp \cos \left(\frac{r\pi}{N+1} \right) \right|$ for a mode r .

For a massive mode with mass m_r , the low-energy spectrum is given by

$$\varepsilon_{r,\mathbf{p}} \approx \begin{cases} +\frac{\mathbf{p}^2}{2m_r} & \text{if } t_\perp \cos \left(\frac{r\pi}{N+1} \right) < 0, \\ -\frac{\mathbf{p}^2}{2m_r} & \text{if } t_\perp \cos \left(\frac{r\pi}{N+1} \right) > 0. \end{cases} \quad (11.20)$$

For odd N , the mode with $r = (N + 1)/2$ is massless and its energy is given by

$$\varepsilon_{\mathbf{p}}^{\pm} = \pm v|\mathbf{p}|. \quad (11.21)$$

Therefore, the low-energy spectrum with odd number of layers is a combination of one massless Dirac mode and $N - 1$ massive Dirac modes per spin and valley. For even number of layers, all N modes are massive at low energies.

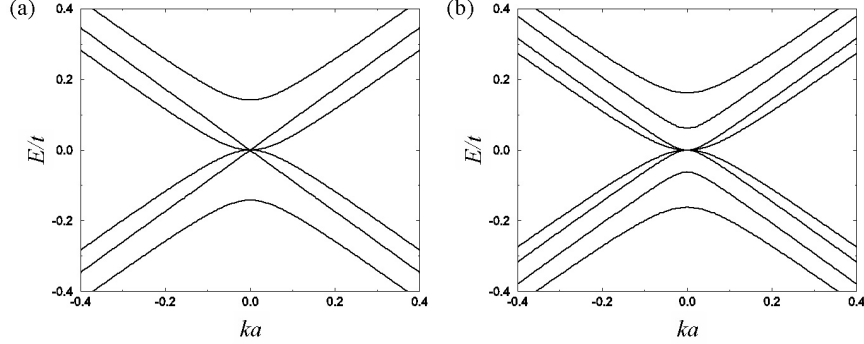


Fig. 11.4. Energy band structure near the K point for AB-stacked (a) trilayer and (b) tetralayer graphene with $t = 3$ eV and $t_{\perp} = 0.1t$.

Fig. 11.4 shows the band structure of AB-stacked trilayer and tetralayer graphene near the K point. As discussed earlier, the trilayer has one massless mode and two massive modes, while the tetralayer has all massive modes at low energies per spin and valley. Note that at $\mathbf{p} = 0$, each massless mode gives two zero energies while each massive mode gives one zero energy. Therefore, for odd N , there are $2 + (N - 1) = N + 1$ zero-energy states, while for even N , there are N zero-energy states per spin and valley.

11.2.5 ABC stacking

In the case of ABC stacking, there is vertical hopping between all the lower layer β sites and all the upper layer α sites. Thus, the Hamiltonian at K in the $(\alpha_1, \beta_1, \alpha_2, \beta_2, \dots)$ basis is given by

$$H_{\text{ABC}}(\mathbf{p}) = \begin{pmatrix} 0 & v\pi^{\dagger} & 0 & 0 & 0 & 0 \\ v\pi & 0 & t_{\perp} & 0 & 0 & 0 \\ 0 & t_{\perp} & 0 & v\pi^{\dagger} & 0 & 0 \\ 0 & 0 & v\pi & 0 & t_{\perp} & 0 & \cdots \\ 0 & 0 & 0 & t_{\perp} & 0 & v\pi^{\dagger} \\ 0 & 0 & 0 & 0 & v\pi & 0 \\ & & & \dots & & \end{pmatrix}. \quad (11.22)$$

Unfortunately for ABC stacking, there do not exist low-order difference equations with a simple boundary condition, but it is still possible to derive a low-energy effective Hamiltonian.

For $\mathbf{p} = 0$ each $\beta - \alpha$ pair forms a symmetric-antisymmetric doublet with energies $\pm t_\perp$, leaving the bottom α_1 and top β_N sites as the only low-energy states. It is possible to construct a 2×2 effective Hamiltonian for the low-energy part of the spectrum using perturbation theory. The same procedure can then be extended to arbitrary stacking sequences. More detailed discussion of the low-energy effective theory is presented in Sec. 11.4.

The simplest example is bilayer graphene. Low and high energy subspaces are identified by finding the spectrum at $\mathbf{p} = 0$ and identifying all the zero-energy eigenstates. The intralayer tunneling term, which is proportional to π or π^\dagger , couples low and high energy states. Using degenerate state perturbation theory, the effective Hamiltonian in the low energy space is given by [39]

$$H_2^{eff}(\mathbf{p}) = - \begin{pmatrix} 0 & \frac{(\pi^\dagger)^2}{2m} \\ \frac{(\pi)^2}{2m} & 0 \end{pmatrix} = -t_\perp \begin{pmatrix} 0 & (\nu^\dagger)^2 \\ (\nu)^2 & 0 \end{pmatrix}, \quad (11.23)$$

where we have used a (α_1, β_2) basis, $m = t_\perp/2v^2$ and $\nu = v\pi/t_\perp$.

In the same way, the effective Hamiltonian of ABC-stacked N -layer graphene in the (α_1, β_N) basis is

$$H_N^{eff}(\mathbf{p}) = -t_\perp \begin{pmatrix} 0 & (\nu^\dagger)^N \\ (\nu)^N & 0 \end{pmatrix}, \quad (11.24)$$

which turns out to be a pseudospin Hamiltonian with the chirality N , as is discussed in Sec. 11.4. Note that for mathematical convenience we have chosen a gauge in which a minus sign appears in front of t_\perp .

Eq. 11.24 can be proven by the mathematical induction method. Imagine that adding one more layer on top of N -layer graphene with ABC stacking. Then the combined Hamiltonian is given by

$$H_{N+1}^{eff}(\mathbf{p}) = -t_\perp \begin{pmatrix} 0 & (\nu^\dagger)^N & 0 & 0 \\ (\nu)^N & 0 & -1 & 0 \\ 0 & -1 & 0 & \nu^\dagger \\ 0 & 0 & \nu & 0 \end{pmatrix}, \quad (11.25)$$

using the $(\alpha_1, \beta_N, \alpha_{N+1}, \beta_{N+1})$ basis.

Let P be a low-energy subspace spanned by (α_1, β_{N+1}) and Q be a high-energy subspace spanned by (α_{N+1}, β_N) . Note that the effective Hamiltonian for $v|\mathbf{p}| \ll t_\perp$ can be derived using the degenerate state perturbation theory [41],

$$H_{eff} \approx H_{PP} - H_{PQ} \frac{1}{H_{QQ}} H_{QP}. \quad (11.26)$$

Here the Hamiltonian matrices projected to P and Q subspace are given by

$$H_{QQ}(\mathbf{p}) = t_{\perp} \begin{pmatrix} 0 & 1 \\ 1 & 0 \end{pmatrix}, H_{PQ}(\mathbf{p}) = -t_{\perp} \begin{pmatrix} 0 & (\nu^{\dagger})^N \\ \nu & 0 \end{pmatrix}, \quad (11.27)$$

and $H_{PP}(\mathbf{p}) = 0$. Thus,

$$H_{N+1}^{eff}(\mathbf{p}) \approx -t_{\perp} \begin{pmatrix} 0 & (\nu^{\dagger})^{N+1} \\ (\nu)^{N+1} & 0 \end{pmatrix}, \quad (11.28)$$

which proves Eq. 11.24. The corresponding energy spectrum in Eq. 11.24 is given by

$$\varepsilon_{eff,\mathbf{p}}^{\pm} = \pm t_{\perp} \left(\frac{v|\mathbf{p}|}{t_{\perp}} \right)^N. \quad (11.29)$$

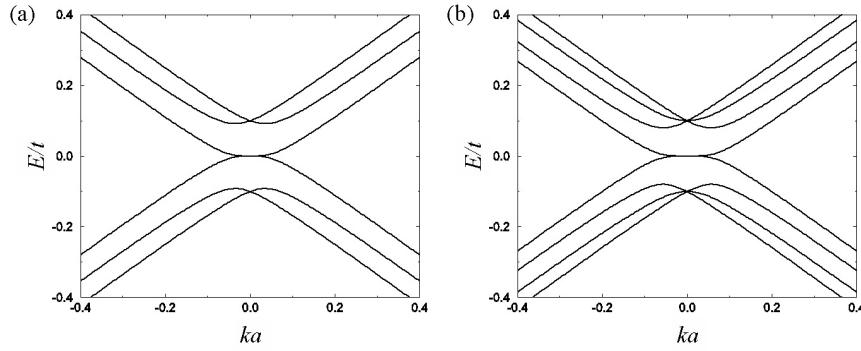


Fig. 11.5. Energy band structure near the K point for ABC-stacked (a) trilayer and (b) tetralayer graphene with $t = 3$ eV and $t_{\perp} = 0.1t$.

Fig. 11.5 shows the band structure of ABC-stacked trilayer and tetralayer graphene near the K point. Note that at $\mathbf{p} = 0$, there are only two zero energy states per spin and valley no matter how thick the stack is.

11.2.6 Arbitrary stacking

It is easy to generalize the previous discussion to construct the Hamiltonian for an arbitrarily stacked multilayer graphene system. The intralayer Hamiltonian at K for i th layer is given by

$$H_{ii}(\mathbf{p}) = \begin{pmatrix} 0 & v\pi^{\dagger} \\ v\pi & 0 \end{pmatrix}. \quad (11.30)$$

The interlayer Hamiltonian between i and $i + 1$ layers is given by

$$H_{i\ i+1}(\mathbf{p}) = \begin{cases} H_{AA}^{\text{inter}} & \text{if AA, BB or CC stacking,} \\ H_{AB}^{\text{inter}} & \text{if AB, BC or CA stacking,} \\ H_{AC}^{\text{inter}} & \text{if AC, CB or BA stacking,} \end{cases} \quad (11.31)$$

where

$$H_{AA}^{\text{inter}}(\mathbf{p}) = \begin{pmatrix} t_{\perp} & 0 \\ 0 & t_{\perp} \end{pmatrix}, H_{AB}^{\text{inter}}(\mathbf{p}) = \begin{pmatrix} 0 & 0 \\ t_{\perp} & 0 \end{pmatrix}, \text{ and } H_{AC}^{\text{inter}}(\mathbf{p}) = \begin{pmatrix} 0 & t_{\perp} \\ 0 & 0 \end{pmatrix}. \quad (11.32)$$

Then the Hamiltonian at K for an arbitrary stacking in the $(\alpha_1, \beta_1, \alpha_2, \beta_2, \dots)$ basis is given by

$$H(\mathbf{p}) = \begin{pmatrix} H_{11} & H_{12} & 0 & 0 & 0 & 0 \\ H_{21} & H_{22} & H_{23} & 0 & 0 & 0 \\ 0 & H_{32} & H_{33} & H_{34} & 0 & 0 \\ 0 & 0 & H_{43} & H_{44} & H_{45} & 0 \\ 0 & 0 & 0 & H_{54} & H_{55} & H_{56} \\ 0 & 0 & 0 & 0 & H_{65} & H_{66} \\ \vdots & \vdots & \vdots & \vdots & \vdots & \vdots \end{pmatrix}, \quad (11.33)$$

where $H_{i+1\ i} = H_i^{\dagger}{}_{i+1}$.

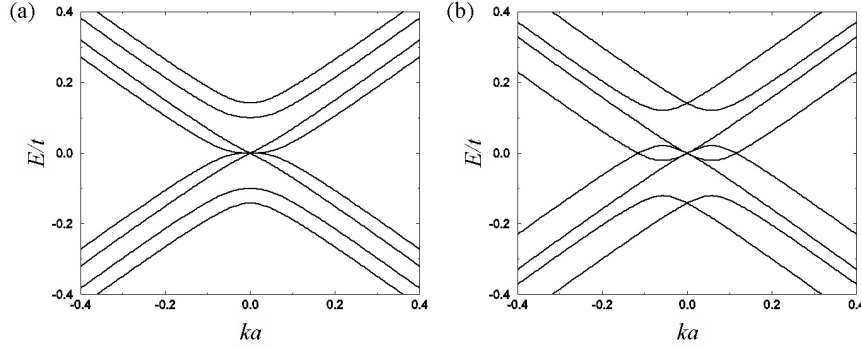


Fig. 11.6. Energy band structure near the K point for (a) ABCB-stacked and (b) ABBC-stacked tetralayer graphene with $t = 3$ eV and $t_{\perp} = 0.1t$.

Fig. 11.6 shows the band structure of ABCB-stacked tetralayer graphene and ABBC-stacked tetralayer graphene near the K point. For ABCB-stacked tetralayer graphene, the low-energy spectrum looks like a superposition of a linear dispersion and a cubic one. For ABBA-stacked tetralayer graphene, zero energies appear not only at the Dirac point but also away from it. A more detailed low-energy spectrum analysis is presented in Sec. 11.4.

11.3 Landau level spectrum

11.3.1 Preliminaries

In the presence of a magnetic field $\mathbf{B} = B\hat{z}$, a Hamiltonian is modified by $\mathbf{p} \rightarrow \mathbf{p} + \frac{e}{c}\mathbf{A}$, where \mathbf{A} is the vector potential with $\mathbf{B} = \nabla \times \mathbf{A}$. The quantum

Hamiltonian is most easily diagonalized by introducing raising and lowering operators, $a = \ell\pi^\dagger/\sqrt{2\hbar}$ and $a^\dagger = \ell\pi/\sqrt{2\hbar}$, where $\ell = \sqrt{\hbar c/e|B|}$, and noting that $[a, a^\dagger] = 1$. Then the wavefunction amplitude on each sublattice of each layer is expanded in terms of parabolic band Landau level states $|n\rangle$ which are eigenstates of $a^\dagger a$. For many Hamiltonians, including those studied here, the Hamiltonian can be block-diagonalized by fixing the parabolic band Landau-level offset between different sublattices and between different layers.

11.3.2 AA stacking

In the case of AA stacking, choose the n -th Landau level basis at K as $(\alpha_{1,n-1}, \beta_{1,n}, \dots, \alpha_{N,n-1}, \beta_{N,n})$. Then Eq. 11.10 reduces to

$$H_{AA}(n) = \begin{pmatrix} 0 & \varepsilon_n & t_\perp & 0 & 0 & 0 \\ \varepsilon_n & 0 & 0 & t_\perp & 0 & 0 \\ t_\perp & 0 & 0 & \varepsilon_n & t_\perp & 0 \\ 0 & t_\perp & \varepsilon_n & 0 & 0 & t_\perp \cdots \\ 0 & 0 & t_\perp & 0 & 0 & \varepsilon_n \\ 0 & 0 & 0 & t_\perp & \varepsilon_n & 0 \\ & & & \cdots & & \end{pmatrix}, \quad (11.34)$$

where $\varepsilon_n = \sqrt{2n\hbar}v/l$. Note that 2D Landau level states with a negative index do not exist so the corresponding basis states and matrix elements are understood as being absent in the matrix block. Thus, $H_{AA}(n=0)$ is a $N \times N$ matrix, while $H_{AA}(n>0)$ is a $2N \times 2N$ matrix.

Diagonalizing Eq. 11.34 using the difference equation method gives the exact Landau level spectrum. For $n > 0$, Landau levels are

$$\varepsilon_{r,n}^\pm = \pm\varepsilon_n + 2t_\perp \cos\left(\frac{r\pi}{N+1}\right), \quad (11.35)$$

where $r = 1, 2, \dots, N$. Note that for $n = 0$, Landau levels are given by $\varepsilon_{r,0} = 2t_\perp \cos\left(\frac{r\pi}{N+1}\right)$. Thus for odd N , there exists one (B -independent) zero-energy Landau level at $r = (N+1)/2$ per spin and valley.

Fig. 11.7 shows the Landau levels of AA-stacked trilayer and tetralayer graphene as a function of magnetic field. For the trilayer, there is one zero-energy Landau level, while for the tetralayer, there is no zero-energy Landau level. Note that there are Landau levels crossing the zero-energy line in AA stacking.

11.3.3 AB stacking

In the case of AB stacking, a proper choice of the n -th Landau level basis at K is $(\alpha_{1,n-1}, \beta_{1,n}, \alpha_{2,n}, \beta_{2,n+1}, \alpha_{3,n-1}, \beta_{3,n}, \alpha_{4,n}, \beta_{4,n+1}, \dots)$ such that all the

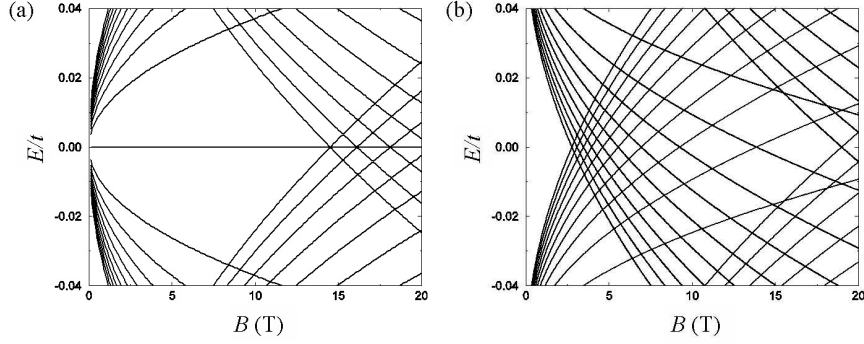


Fig. 11.7. Landau levels of AA-stacked (a) trilayer and (b) tetralayer graphene with $t = 3$ eV and $t_{\perp} = 0.1t$. Landau levels are shown up to $n = 10$.

interlayer hopping terms are contained in the n -th Landau level Hamiltonian. Then Eq. 11.14 reduces to

$$H_{AB}(n) = \begin{pmatrix} 0 & \varepsilon_n & 0 & 0 & 0 & 0 \\ \varepsilon_n & 0 & t_{\perp} & 0 & 0 & 0 \\ 0 & t_{\perp} & 0 & \varepsilon_{n+1} & 0 & t_{\perp} \\ 0 & 0 & \varepsilon_{n+1} & 0 & 0 & 0 \\ 0 & 0 & 0 & 0 & 0 & \varepsilon_n \\ 0 & 0 & t_{\perp} & 0 & \varepsilon_n & 0 \\ & & & \dots & & \end{pmatrix}. \quad (11.36)$$

As discussed in Sec. 11.3.2, special care should be given for states with a negative index.

For the Hamiltonian in Eq. 11.36, there do not exist corresponding difference equations with a proper boundary condition, thus cannot be diagonalized analytically. From Eq. 11.23, however, the low-energy Landau levels for massive mode with mass m_r can be obtained as

$$\varepsilon_{r,n} \approx \begin{cases} +\hbar\omega_r\sqrt{n(n+1)} & \text{if } t_{\perp} \cos\left(\frac{r\pi}{N+1}\right) < 0, \\ -\hbar\omega_r\sqrt{n(n+1)} & \text{if } t_{\perp} \cos\left(\frac{r\pi}{N+1}\right) > 0, \end{cases} \quad (11.37)$$

where $r = 1, 2, \dots, N$ and $\omega_r = e|B|/m_r c$, which is proportional to B . These equations apply at small B , just as the low-energy dispersions for $B = 0$ applied at small momentum \mathbf{p} . For the massless mode, from Eq. 11.21 Landau levels are given by

$$\varepsilon_n^{\pm} = \pm\varepsilon_n, \quad (11.38)$$

which is proportional to $B^{1/2}$.

Fig. 11.8 shows the Landau levels of AB-stacked trilayer and tetralayer graphene as a function of magnetic field. Note that the linear B dependence

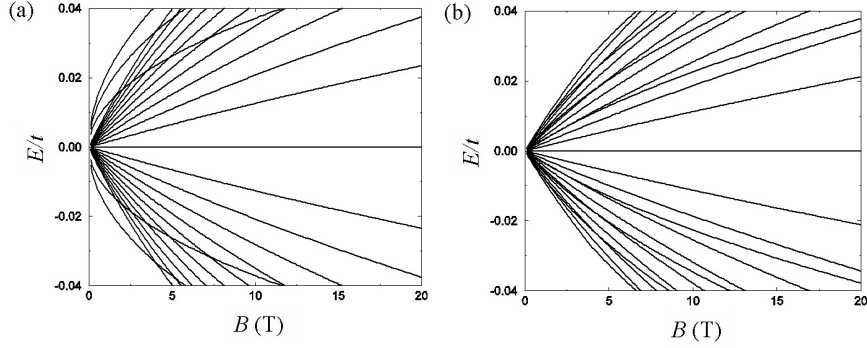


Fig. 11.8. Landau levels of AB-stacked (a) trilayer and (b) tetralayer graphene with $t = 3$ eV $t_{\perp} = 0.1t$. Landau levels are shown up to $n = 10$.

expected for massive modes applies over a more limited field range when the mass is small. For the trilayer, Landau levels are composed of massless Dirac spectra ($\propto B^{1/2}$) and massive Dirac spectra ($\propto B$), while for the tetralayer, Landau levels are all massive Dirac spectra. This is consistent with the band structure analysis shown in Fig. 11.4.

Note that the massive modes in Eq. 11.37 have two zero-energy Landau levels for $n = -1$ and 0 , whereas the massless mode in Eq. 11.38 has one for $n = 0$. There are therefore N zero-energy Landau levels per spin and valley in both even and odd N AB stacks. This property can also be understood directly from the Hamiltonian in Eq. 11.36, by eliminating negative n basis states and rearranging rows to block-diagonalize the matrix.

11.3.4 ABC stacking

In the case of ABC stacking, a proper choice of the n -th Landau level basis at K is $(\alpha_{1,n-1}, \beta_{1,n}, \alpha_{2,n}, \beta_{2,n+1}, \alpha_{3,n+1}, \beta_{3,n+2}, \dots)$ such that all the interlayer hopping terms are contained in the n -th Landau level Hamiltonian. Then Eq. 11.22 reduces to

$$H_{\text{ABC}}(n) = \begin{pmatrix} 0 & \varepsilon_n & 0 & 0 & 0 & 0 \\ \varepsilon_n & 0 & t_{\perp} & 0 & 0 & 0 \\ 0 & t_{\perp} & 0 & \varepsilon_{n+1} & 0 & 0 \\ 0 & 0 & \varepsilon_{n+1} & 0 & t_{\perp} & 0 & \dots \\ 0 & 0 & 0 & t_{\perp} & 0 & \varepsilon_{n+2} \\ 0 & 0 & 0 & 0 & \varepsilon_{n+2} & 0 \\ \dots & & & & & \end{pmatrix}. \quad (11.39)$$

As discussed in Sec. 11.3.2, special care should be given for states with a negative index.

The low-energy spectrum can be obtained from the effective Hamiltonian in Eq. 11.24. For $n > 0$, Landau levels are given by

$$\varepsilon_n^\pm = \pm \hbar \omega_N \sqrt{n(n+1) \cdots (n+N-1)}, \quad (11.40)$$

where $\hbar \omega_N = t_\perp (\sqrt{2} \hbar v / t_\perp l)^N \propto B^{N/2}$, while for $n = -N+1, -N+2, \dots, 0$ they are zero. Note that there are N zero-energy Landau levels per spin and valley for ABC-stacked N -layer graphene.

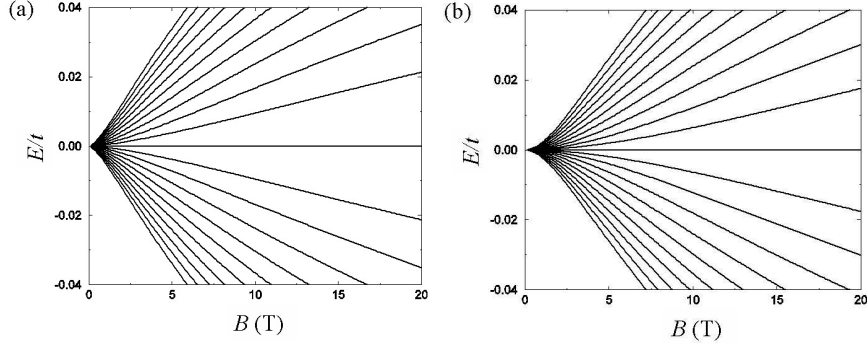


Fig. 11.9. Landau levels of ABC-stacked (a) trilayer and (b) tetralayer graphene with $t = 3$ eV and $t_\perp = 0.1t$. Landau levels are shown up to $n = 10$.

Fig. 11.9 shows the Landau levels of ABC-stacked trilayer and tetralayer graphene as a function of magnetic field. For the trilayer, Landau levels are proportional to $B^{3/2}$, while for the tetralayer, Landau levels are proportional to B^2 at low energies.

11.3.5 Arbitrary stacking

It is straightforward to generalize the previous discussion to construct the Hamiltonian in the Landau level basis for an arbitrarily stacked multilayer graphene system. As seen in Eqs. 11.34, 11.36 and 11.39, it is possible to make the Hamiltonian block-diagonal by properly choosing the Landau level basis.

Let's assume that the n -th Landau level basis at K for the i th layer is $(\alpha_{i,n-1}, \beta_{i,n})$. Then the basis for $i+1$ th layer is

$$\begin{cases} (\alpha_{i+1,n-1}, \beta_{i+1,n}) & \text{if AA, BB or CC stacking,} \\ (\alpha_{i+1,n}, \beta_{i+1,n+1}) & \text{if AB, BC or CA stacking,} \\ (\alpha_{i+1,n-2}, \beta_{i+1,n-1}) & \text{if AC, CB or BA stacking,} \end{cases} \quad (11.41)$$

between i and $i+1$ layers. As discussed in Sec. 11.3.2, special care should be given for states with a negative index.

Fig. 11.10 shows Landau levels of ABCB-stacked tetralayer graphene and ABBC-stacked tetralayer graphene. For the ABCB-stacked tetralayer

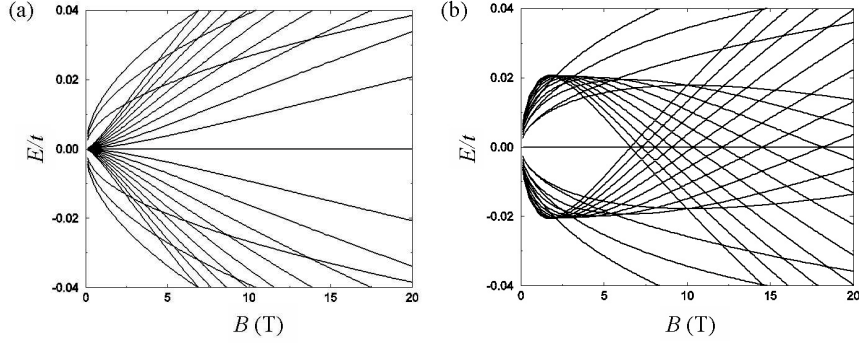


Fig. 11.10. Landau levels of (a) ABCB-stacked and (b) ABBC-stacked tetralayer graphene with $t = 3$ eV and $t_{\perp} = 0.1t$. Landau levels are shown up to $n = 10$.

graphene, the Landau levels at low energies look like a superposition of $B^{1/2}$ and $B^{3/2}$ levels, which is consistent with Fig. 11.6(a). For the ABBA-stacked tetralayer graphene, there are Landau levels crossing the zero-energy line, which is consistent with Fig. 11.6(b). Detailed low-energy Landau-level spectrum analysis is presented in Sec. 11.4.

11.4 Low-energy effective theory

11.4.1 Introduction

In monolayer graphene, there are two sublattices, α and β in a unit cell and wavefunctions are described by the amplitudes on each sublattice. In bilayer graphene, there are, in addition, top and bottom layer degrees of freedom and wavefunctions at low energies have two components localized on one of the sublattices in each layer. The two component wavefunctions in graphene are very similar to the spinor wavefunctions of real spins and are frequently referred to as a *pseudospin*. *Chirality* is formally defined as a projection of pseudospin on the direction of motion [3]. It is known that monolayer graphene is described by a pseudospin doublet with chirality one while bilayer graphene is described by a pseudospin doublet with chirality two. Below, we consider the meaning of this statement and its natural extension to arbitrarily stacked multilayer graphene.

In this section, we present the low-energy effective theory of arbitrarily stacked multilayer graphene using a degenerate state perturbation theory. We demonstrate an unanticipated low-energy property of graphene multilayers, which follows from an interplay between interlayer tunneling and the chiral properties of low-energy quasiparticles in an isolated graphene sheet. The low-energy band structure of multilayer graphene consists of a set of independent

pseudospin doublets and its chirality sum is given by the number of layers [20, 21].

11.4.2 Pseudospin Hamiltonian

First, define a pseudospin Hamiltonian which describes 2D chiral quasiparticles. A pseudospin Hamiltonian with the chirality index J is of the form

$$\begin{aligned} H_J(\mathbf{p}) &= t_\perp \begin{pmatrix} 0 & (\nu_{\mathbf{p}}^\dagger)^J \\ (\nu_{\mathbf{p}})^J & 0 \end{pmatrix} \\ &= t_\perp \left(\frac{v^*|\mathbf{p}|}{t_\perp} \right)^J [\cos(J\phi_{\mathbf{p}}) \sigma_x + \sin(J\phi_{\mathbf{p}}) \sigma_y] \end{aligned} \quad (11.42)$$

where $\nu_{\mathbf{p}} \equiv v^*|\mathbf{p}|e^{i\phi_{\mathbf{p}}}/t_\perp$, σ_α is a Pauli matrix acting on the doublet pseudospin and $\phi_{\mathbf{p}} = \tan^{-1}(p_y/p_x)$ is the orientation of \mathbf{p} . v^* is the effective in-plane Fermi velocity (for example, $v^* = v$ for $J = 1$ monolayer and $J = 2$ bilayer graphene, and in general for periodic ABC stacking). Note that quasiparticles described by the pseudospin Hamiltonian with chirality J acquire a Berry phase $J\pi$ upon an adiabatic evolution along a closed orbit, which can be viewed as rotation of the pseudospin by an angle $J\pi$ [39].

The Hamiltonian has a simple energy spectrum given by

$$\varepsilon_{s,\mathbf{p}} = st_\perp \left(\frac{v^*|\mathbf{p}|}{t_\perp} \right)^J \quad (11.43)$$

and corresponding eigenfunctions are

$$|s, \mathbf{p}\rangle = \frac{1}{\sqrt{2}} \begin{pmatrix} s \\ e^{iJ\phi_{\mathbf{p}}} \end{pmatrix} \quad (11.44)$$

where $s = \pm 1$ for positive (negative) energy states, respectively.

11.4.3 Stacking diagrams

When sheets are stacked to form a multilayer system, there is an energetic preference for an arrangement in which each layer is rotated by 60° with respect to one of the two sublattices of its neighbors [40]. This prescription generates 2^{N-2} ($N > 1$) distinct N -layer sequences if we exclude consecutive stacking (such as AA, BB or CC). We refer to multilayers in this class as *normal*. For the analysis of low-energy effective theory, we only consider the normal stacking and discuss the effects of the consecutive stacking later.

When a B layer is placed on an A layer, a C layer on a B layer, or an A layer on a C layer, the α sites of the upper layer are above the β sites of the lower layer and therefore linked by the nearest-neighbor interlayer π -orbital hopping amplitude t_\perp . For the corresponding anticyclic stacking choices (A

on B, B on C, or C on A), it is the β sites of the upper layer and the α sites of the lower layer that are linked. All distinct normal stacking sequences with $N = 3, 4$ and 5 layers are illustrated in Fig. 11.11, in which we have arbitrarily labeled the first two layers starting from the bottom as A and B.

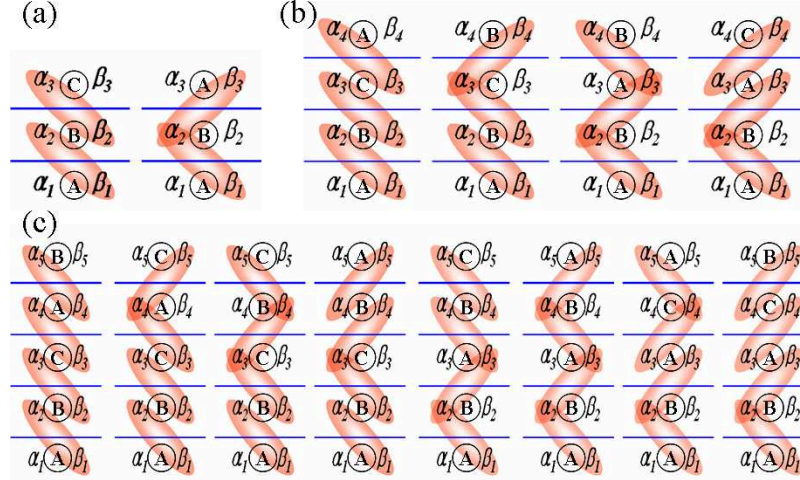


Fig. 11.11. All normal stacking sequences and linkage diagrams for $N = 3, 4$ and 5 layers in (a), (b) and (c), respectively. Shaded ovals link α and β nearest-neighbor interlayers.

11.4.4 Partitioning rules

The low-energy band and Landau level structure can be read off the stacking diagrams illustrated in Fig. 11.11 by partitioning a stack using the following rules, which are justified in the following section.

(i) Identify the longest nonoverlapping segments within which there are no reversals of stacking sense. When there is ambiguity in the selection of nonoverlapping segments, choose the partitioning which incorporates the largest number of layers. Each segment defines a J -layer partition of the stack and may be associated with a chirality J doublet.

(ii) Iteratively partition the remaining segments of the stack into smaller J elements, excluding layers contained within previously identified partitions, until all layers are exhausted.

Because each layer is a member of one and only one partition, the partitioning rules imply that the chirality sum in an N -layer stack is given by

$$\sum_{i=1}^{N_D} J_i = N \quad (11.45)$$

where N_D is the number of pseudospin doublets. Note that N_D depends on the details of the stacking sequence and is given by half the sum of the number of isolated sites and the number of odd-length chains.

The chirality decompositions which follow from these rules are summarized in Table 11.1. Note that when each added layer cycles around the stacking triangle of Fig. 11.1(b) in the same rotational sense, the chirality increases. Reversals of the rotational sense tend to increase N_D . Although chiralities are decomposed depending on the stacking sequence, the chirality sum is conserved and given by the number of layers.

In applying these rules, the simplest case is repeated ABC stacking for which there are no stacking sense reversals and therefore a single $J = N$ partition. In the opposite limit, repeated AB stacking, the stacking sense is reversed in every layer and the rules imply $N/2$ partitions with $J = 2$ for even N , and when N is odd a remaining $J = 1$ partition.

Between these two limits, a rich variety of qualitatively distinct low-energy behaviors occur. For example, in the ABCB-stacked tetralayer, ABC is identified as a $J = 3$ doublet and the remaining B layer gives a $J = 1$ doublet. The low-energy band structure and the Landau level structure of this stack, as illustrated in Figs. 11.6(a) and 11.10(a), have two sets of low-energy bands with $|E| \propto k, k^3$, Landau levels with $|E| \propto B^{1/2}, B^{3/2}$, and four zero-energy Landau levels per spin and valley. All these properties are predicted by the partitioning rules.

Table 11.1. Chirality decomposition for $N = 3, 4, 5, 6$ layer stacks.

stacking	chirality	stacking	chirality
ABC	3	ABCABC	6
ABA	$2 \oplus 1$	ABCABA	$5 \oplus 1$
		ABCACA	$4 \oplus 2$
ABCA	4	ABCACB	$4 \oplus 2$
ABCB	$3 \oplus 1$	ABCBCA	$3 \oplus 3$
ABAB	$2 \oplus 2$	ABCBCB	$3 \oplus 2 \oplus 1$
ABAC	$1 \oplus 3$	ABCBAB	$3 \oplus 2 \oplus 1$
		ABCBAC	$3 \oplus 3$
ABCAB	5	ABABCA	$2 \oplus 4$
ABCAC	$4 \oplus 1$	ABABCB	$2 \oplus 3 \oplus 1$
ABCBC	$3 \oplus 2$	ABABAB	$2 \oplus 2 \oplus 2$
ABCBA	$3 \oplus 2$	ABABAC	$2 \oplus 1 \oplus 3$
ABABC	$2 \oplus 3$	ABACAB	$2 \oplus 1 \oplus 3$
ABABA	$2 \oplus 2 \oplus 1$	ABACAC	$1 \oplus 3 \oplus 2$
ABACA	$1 \oplus 3 \oplus 1$	ABACBC	$1 \oplus 4 \oplus 1$
ABACB	$1 \oplus 4$	ABACBA	$1 \oplus 5$

11.4.5 Degenerate state perturbation theory

This approach starts from the well-known $J = 1$ massless Dirac equation [1, 2] $\mathbf{k} \cdot \mathbf{p}$ model for isolated sheets,

$$H_{\text{MD}}(\mathbf{p}) = - \begin{pmatrix} 0 & v\pi^\dagger \\ v\pi & 0 \end{pmatrix}, \quad (11.46)$$

where $\pi = p_x + ip_y$ and v is the quasiparticle velocity. (For mathematical convenience we have chosen a gauge in which a minus sign appears in the definition.) An N -layer stack has a two-dimensional band structure with $2N$ atoms per unit cell. The Hamiltonian can be written as

$$H = H_\perp + H_\parallel, \quad (11.47)$$

where H_\perp accounts for interlayer tunneling and H_\parallel for intralayer tunneling. H_\parallel is the direct product of massless Dirac model Hamiltonians H_{MD} for the sublattice pseudospin degrees of freedom of each layer. The low-energy Hamiltonian is constructed by first identifying the zero-energy eigenstates of H_\perp and then treating H_\parallel as a perturbation.

Referring to Fig. 11.11, H_\perp is the direct product of a set of finite-length 1D tight-binding chains, as shown in Eq. 11.4, and a null matrix with dimension equal to the number of isolated sites. The set of zero-energy eigenstates of H_\perp consists of the states localized on isolated sites and the single zero-energy eigenstates of each odd-length chain.

The low-energy effective Hamiltonian is evaluated by applying leading order degenerate state perturbation theory to the zero-energy subspace. The matrix element of the effective Hamiltonian between degenerate zero-energy states r and r' is given by [41]

$$\langle \Psi_r | H | \Psi_{r'} \rangle = \langle \Psi_r | H_\parallel \left[\hat{Q}(-H_\perp^{-1})\hat{Q}H_\parallel \right]^{n-1} | \Psi_{r'} \rangle, \quad (11.48)$$

where n is the smallest positive integer for which the matrix element is nonzero, \hat{P} is a projection operator onto the zero-energy subspace and $\hat{Q} = 1 - \hat{P}$.

To understand the structure of this Hamiltonian, let's consider ABC-stacked multilayer graphene and re-derive the low-energy effective Hamiltonian in Eq. 11.24. For ABC-stacked N -layer graphene, the zero-energy states are the two isolated site states in bottom and top layers, α_1 and β_N . $N - 1$ sets of two-site chains form high-energy states. Because H_\parallel is diagonal in layer index and H_\perp (and hence H_\perp^{-1}) can change the layer index by one unit, the lowest order at which α_1 and β_N are coupled is $n = N$.

According to Eq. 11.4, the wavefunction of each two-site chain is given by

$$|\Phi_{\sigma_r}\rangle = \frac{1}{\sqrt{2}}(|\beta_r\rangle + \sigma_r |\alpha_{r+1}\rangle), \quad (11.49)$$

with the energy $\varepsilon_r = t_\perp \sigma_r$, where $\sigma_r = \pm 1$ and $r = 1, 2, \dots, N-1$. From Eq. 11.48,

$$\begin{aligned}
\langle \alpha_1 | H | \beta_N \rangle &= \langle \alpha_1 | H_\parallel \left[\hat{Q}(-H_\perp^{-1}) \hat{Q} H_\parallel \right]^{N-1} | \beta_N \rangle \\
&= \sum_{\{\sigma_r\}} \frac{\langle \alpha_1 | H_\parallel | \Phi_{\sigma_1} \rangle \cdots \langle \Phi_{\sigma_{N-1}} | H_\parallel | \beta_N \rangle}{(-\varepsilon_1) \cdots (-\varepsilon_{N-1})} \\
&= -t_\perp \sum_{\{\sigma_r\}} \frac{(-\sigma_1/2) \cdots (-\sigma_{N-1}/2)}{(-\sigma_1) \cdots (-\sigma_{N-1})} (\nu^\dagger)^N \\
&= -t_\perp (\nu^\dagger)^N \sum_{\sigma_1, \dots, \sigma_{N-1}} \frac{1}{2^{N-1}} \\
&= -t_\perp (\nu^\dagger)^N, \tag{11.50}
\end{aligned}$$

where $\nu = v\pi/t_\perp$. Here $\langle \alpha_1 | H_\parallel | \Phi_{\sigma_1} \rangle = -(1/\sqrt{2})t_\perp \nu^\dagger$, $\langle \Phi_{\sigma_{N-1}} | H_\parallel | \beta_N \rangle = -(\sigma_{N-1}/\sqrt{2})t_\perp \nu^\dagger$ and $\langle \Phi_{\sigma_r} | H_\parallel | \Phi_{\sigma_{r+1}} \rangle = -(\sigma_r/2)t_\perp \nu^\dagger$ were used. Thus, the effective Hamiltonian of N -layer graphene with ABC stacking has a single $J = N$ pseudospin doublet given by

$$H_N^{eff} = -t_\perp \begin{pmatrix} 0 & (\nu^\dagger)^N \\ (\nu)^N & 0 \end{pmatrix}. \tag{11.51}$$

A more complex but representative example is realized by placing a single reversed layer on top of ABC-stacked N -layer graphene with $N > 2$. Note that the last chain has three sites, thus it has a zero-energy state β_{N+1}^- defined by

$$|\beta_{N+1}^- \rangle = \frac{1}{\sqrt{2}} (|\beta_{N+1} \rangle - |\beta_{N-1} \rangle), \tag{11.52}$$

and two high-energy states with energies $\sqrt{2}\sigma_{N-1}t_\perp$ defined by

$$|\Phi_{\sigma_{N-1}} \rangle = \frac{1}{2} |\beta_{N-1} \rangle + \frac{\sigma_{N-1}}{\sqrt{2}} |\alpha_N \rangle + \frac{1}{2} |\beta_{N+1} \rangle, \tag{11.53}$$

where $\sigma_{N-1} = \pm 1$. Then the first-order perturbation theory gives

$$\langle \alpha_{N+1} | H | \beta_{N+1}^- \rangle = -\frac{t_\perp}{\sqrt{2}} \nu^\dagger, \tag{11.54}$$

suggesting the existence of the massless Dirac mode with a *reduced* velocity.

As in Eq. 11.50, the result is

$$H_{N+1}^{eff} = -t_\perp \begin{pmatrix} 0 & \frac{\nu^\dagger}{\sqrt{2}} & 0 & \frac{(\nu^\dagger)^2}{2} \\ \frac{\nu}{\sqrt{2}} & 0 & -\frac{(\nu)^{N-1}}{\sqrt{2}} & 0 \\ 0 & -\frac{(\nu^\dagger)^{N-1}}{\sqrt{2}} & 0 & \frac{(\nu^\dagger)^N}{2} \\ \frac{\nu^2}{2} & 0 & \frac{(\nu)^N}{2} & 0 \end{pmatrix}, \tag{11.55}$$

using a $(\alpha_{N+1}, \beta_{N+1}^-, \alpha_1, \beta_N)$ basis. The first 2×2 block in Eq. 11.55 gives a $J = 1$ doublet with a reduced velocity. The matrix in Eq. 11.55 is not block-diagonal thus the second 2×2 matrix block is not obviously a N -chiral system. The $J = N$ doublet in this instance includes both the (α_1, β_N) subspace contribution and an equal contribution due to perturbative coupling to the $(\alpha_{N+1}, \beta_{N+1}^-)$ subspace. Using a similar perturbation theory shown in Eq. 11.26, we can obtain higher order correction by integrating out the massless Dirac mode which forms a higher energy state. Then the final Hamiltonian is reduced to

$$H_{N+1}^{eff} \approx H_1 \oplus H_N, \quad (11.56)$$

where

$$H_1 = -t_\perp \begin{pmatrix} 0 & \nu^\dagger/\sqrt{2} \\ \nu/\sqrt{2} & 0 \end{pmatrix}, \quad H_N = -t_\perp \begin{pmatrix} 0 & (\nu^\dagger)^N \\ (\nu)^N & 0 \end{pmatrix}. \quad (11.57)$$

This means that the combined system can be described by a combination of one 1-chiral system with a reduced velocity and one N -chiral system. Note that stacking a layer with an opposite handedness partitions a system into systems with different chiralities.

Similarly, we can extend the degenerate state perturbation theory to arbitrarily stacked multilayer graphene [20, 21]. Then, the effective Hamiltonian of any N -layer graphene is given as follows:

$$H_N^{eff} \approx H_{J_1} \oplus H_{J_2} \oplus \cdots \oplus H_{J_{N_D}}, \quad (11.58)$$

with the chirality sum rule in Eq. 11.45.

11.4.6 Limitations of the minimal model

The low-energy effective Hamiltonian has been obtained from the minimal model in which only the nearest-neighbor intralayer tunneling and nearest-neighbor interlayer tunneling are included. The result is valid when contributions from the neglected terms are smaller than the terms in the effective Hamiltonian from the minimal model.

For example, in bilayer graphene, if the interlayer tunneling term $\gamma_3 \approx 0.3$ eV from the $\alpha_1 \rightarrow \beta_2$ hopping process (called trigonal warping) is included, a term with an energy scale $v_3|\mathbf{p}|$ appears in the low-energy effective theory [39], where $\frac{\hbar v_3}{a} = \frac{\sqrt{3}}{2}\gamma_3$. Then the massive-chiral effective Hamiltonian in Eq. 11.23 applies at energies larger than the trigonal-warping scale but still smaller than the interlayer hopping scale,

$$v_3|\mathbf{p}| < \frac{(v|\mathbf{p}|)^2}{t_\perp} < t_\perp. \quad (11.59)$$

11.4.7 Effects of the consecutive stacking

The analysis presented so far is based on the assumption that stacking one layer directly on top of its neighbor (AA, BB or CC stacking) is not allowed. We can still apply a similar diagram analysis and identify the zero-energy states at the Dirac point even if a consecutive stacking exists. In this case, however, zero-energy states can appear not only at the Dirac points but also at other points in momentum space. The degenerate state perturbation theory at the Dirac point discussed so far, therefore, cannot completely capture the low-energy states.

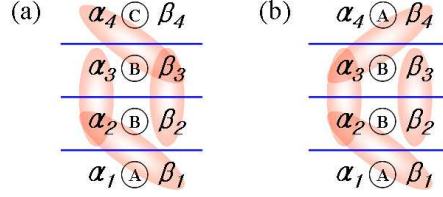


Fig. 11.12. Stacking diagrams for (a) ABBC-stacked and (b) ABBA-stacked tetralayer graphene. Shaded ovals link nearest-neighbor interlayers.

As an example, let us consider ABBC-stacked tetralayer graphene, as illustrated in Fig. 11.12(a). Here, in addition to α_1 and β_4 , there are two zero-energy states at each three-site chain defined by

$$\begin{aligned} |\tilde{\beta}_1\rangle &= \frac{1}{\sqrt{2}} (|\beta_1\rangle - |\alpha_3\rangle), \\ |\tilde{\alpha}_4\rangle &= \frac{1}{\sqrt{2}} (|\alpha_4\rangle - |\beta_2\rangle). \end{aligned} \quad (11.60)$$

Thus the matrix elements between low-energy states are given by

$$\langle \alpha_1 | H | \tilde{\beta}_1 \rangle = \langle \tilde{\alpha}_4 | H | \beta_4 \rangle = -\frac{t_\perp}{\sqrt{2}} \nu^\dagger. \quad (11.61)$$

Therefore the system at the Dirac point can be described by two massless Dirac modes with a reduced velocity, as shown in Figs. 11.6(b) and 11.10(b).

Another example is ABBA-stacked tetralayer graphene, as illustrated in Fig. 11.12(b). In this case, there are two zero-energy states at α_1 and α_4 . The high-energy states Φ_r and corresponding energies ε_r are given by Eq. 11.4 with $N = 4$; thus

$$\langle \alpha_1 | H | \alpha_4 \rangle = \sum_{r=1}^4 \frac{\langle \alpha_1 | H_\parallel | \Phi_r \rangle \langle \Phi_r | H_\parallel | \alpha_4 \rangle}{(-\varepsilon_r)} = -ct_\perp |\nu|^2, \quad (11.62)$$

where $c = \frac{1}{5} \sum_r \sin\left(\frac{r\pi}{5}\right) \sin\left(\frac{4r\pi}{5}\right) / \cos\left(\frac{r\pi}{5}\right) = -1$. Here the low-energy state is composed of one *non-chiral* massive mode. Note that because of the non-chirality, there are no zero-energy Landau levels.

11.5 Applications

11.5.1 Quantum Hall conductivity

Applying the Kubo formula to a disorder-free systems gives the conductivity tensor with an external magnetic field along z ,

$$\sigma_{ij}(\omega) = -\frac{e^2}{2\pi\hbar l_B^2} \sum_n f_n \Omega_{ij}^n(\omega), \quad (11.63)$$

where f_n is Fermi factor of n -th energy state, $i, j = x, y$ and

$$\Omega_{ij}^n(\omega) = i \sum_{m \neq n} \left[\frac{\langle n | \hbar v_i | m \rangle \langle m | \hbar v_j | n \rangle}{(\varepsilon_n - \varepsilon_m)(\varepsilon_n - \varepsilon_m + \hbar\omega + i\eta)} - \frac{\langle m | \hbar v_i | n \rangle \langle n | \hbar v_j | m \rangle}{(\varepsilon_n - \varepsilon_m)(\varepsilon_n - \varepsilon_m - \hbar\omega - i\eta)} \right]. \quad (11.64)$$

Here v_i is a velocity operator obtained by taking a derivative of the Hamiltonian $H(\mathbf{p})$ with respect to p_i . Note that in the case of multilayer graphene, the velocity operator is constant, i.e. it does not depend on the Landau level index.

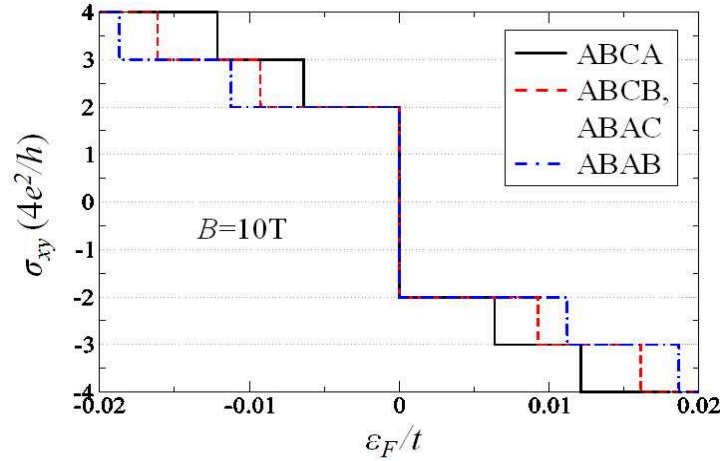


Fig. 11.13. Noninteracting system Hall conductivity as a function of the Fermi energy for all the normal tetralayer graphene stacks when $B = 10$ T, $t = 3$ eV, and $t_{\perp} = 0.1t$. The Hall conductivity calculations shown in this figure assume neutralizing ionized donors spread equally between the four layers.

The appropriate quantized Hall conductivity is obtained by evaluating $\sigma_H = \sigma_{xy}(0)$. In Fig. 11.13, we plot the noninteracting Hall conductivity as a function of Fermi energy for normal tetralayer graphene stacks assuming neutralizing ionized donors spread equally between the four layers. Note that though the positions of jumps in the Hall conductivity are different depending on the stacking sequences, all the normal tetralayers follow the same quantization rule with the large jump between the $\pm(4e^2/h)N/2$ Hall plateaus at $\varepsilon_F = 0$, where $N = 4$ for tetralayers.

It follows from Eq. 11.45 that the Hall conductivity of an N -layer stack has strong integer quantum Hall effects with the following quantization rule,

$$\sigma_{xy} = \pm \frac{4e^2}{h} \left(\frac{N}{2} + n \right), \quad (11.65)$$

where n is a non-negative integer.

Although the minimal model we use includes only the nearest-neighbor intralayer tunneling and nearest-neighbor interlayer tunneling, these results are approximately valid in the broad intermediate magnetic field B range between ≈ 10 T and ≈ 100 T, over which the intralayer hopping energy in the field ($\approx \hbar v/\ell$ where $\ell/\sqrt{|B|} = \sqrt{\hbar c/e} \approx 25.7 \text{ nm}/\sqrt{\text{T}}$ defines the magnetic length ℓ) is larger than the distant neighbor interlayer hopping amplitudes that we have neglected but still smaller than t_\perp . For example, consider the $\alpha_1 \rightarrow \alpha_3$ hopping process in ABA-stacked trilayer with the tunneling term $\gamma_2 \approx -20$ meV [16], then the valid range of magnetic field for the minimal model is given by

$$|\gamma_2| < \frac{(\hbar v/l)^2}{t_\perp} < t_\perp. \quad (11.66)$$

When γ_2 does not play an important role (in $N = 2$ stacks, for example), the lower limit of the validity range is parametrically smaller. The minimum field in bilayers has been estimated to be ≈ 1 T [39], by comparing intralayer hopping with the $\gamma_3 \approx 0.3$ eV interlayer hopping amplitude as in Eq. 11.59,

$$\hbar v_3/l < \frac{(\hbar v/l)^2}{t_\perp} < t_\perp. \quad (11.67)$$

Discussion on the effects of disorder and electron-electron interactions can be found in Refs. [20, 21].

11.5.2 Optical conductivity

One particularly intriguing property of neutral single-layer graphene sheets is the interband optical conductivity [42–45], which is approximately constant over a broad range of frequencies with a value close to

$$\sigma_{uni} = \frac{\pi e^2}{2h}, \quad (11.68)$$

dependent only on fundamental constants of nature. Recently, it was also found [46] that for frequencies in the optical range the conductivity per layer in multilayer graphene sheets is also surprisingly close to σ_{uni} . Here we identify the emergent chiral symmetry of multilayers as a key element of the physics responsible for the ubiquity of σ_{uni} in multilayer graphene systems [28].

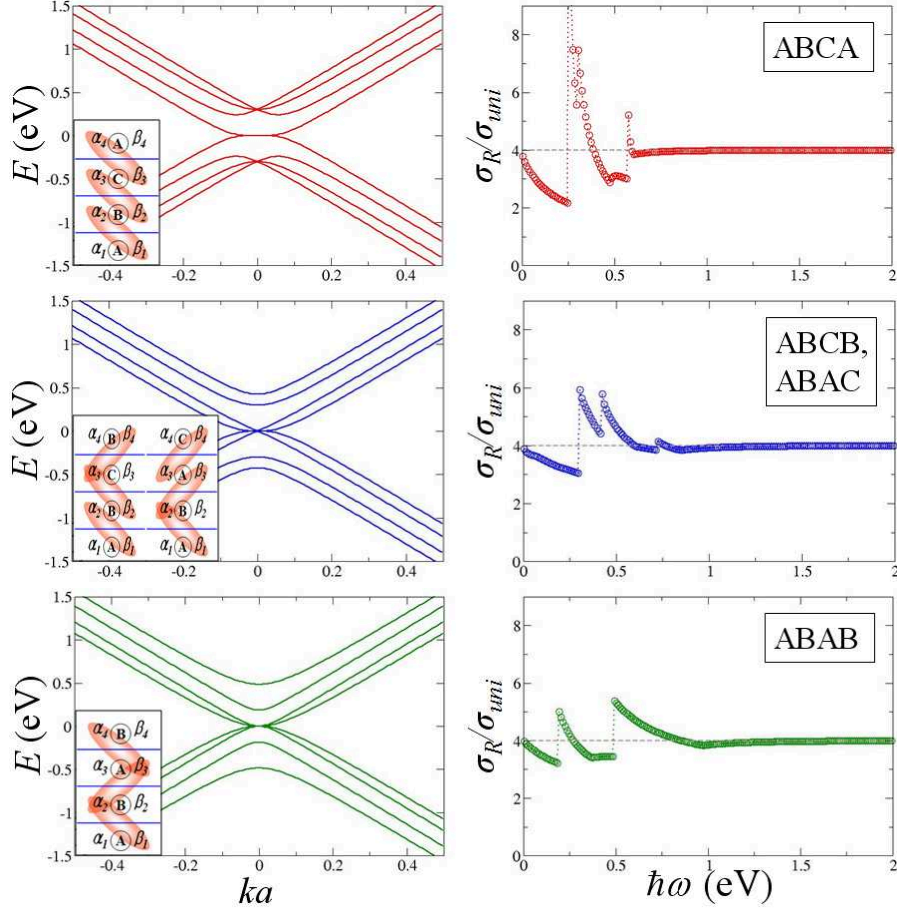


Fig. 11.14. Energy band structure and real part of the conductivity for all the normal tetralayer graphene stacks, ABCA (top), ABCB, ABAC (middle) and ABAB (bottom). The insets show stacking diagrams where shaded ovals link sublattices α and β to the nearest-neighbor interlayers.

The optical conductivity of an N -layer system is expected to approach $N\sigma_{uni}$ for frequencies that exceed the interlayer-coupling scale but are smaller than the π -bandwidth scale, since the layers then contribute independently

and the Dirac model still applies. In the low-energy limit the spectrum separates asymptotically into decoupled pseudospin doublets, each of which has chiral symmetry. The conductivity of a pseudospin doublet with chirality J is $J\sigma_{uni}$. It then follows from the chirality sum rule in Eq. 11.45 that the conductivity of the ideal model also approaches $N\sigma_{uni}$ in the $\omega \rightarrow 0$ limit. Note that the low-frequency limit of the interband conductivity does not result from independent single-layer contributions but has a completely different origin.

The Kubo formula for the real part of the optical conductivity, $\sigma_R(\omega) \equiv \text{Re}[\sigma_{xx}(\omega)]$, of a 2D electron-gas system is

$$\sigma_R(\omega) = -\frac{\pi e^2}{h} \sum_{n \neq n'} \int \frac{d^2k}{2\pi} \frac{f_{n,\mathbf{k}} - f_{n',\mathbf{k}}}{\varepsilon_{n,\mathbf{k}} - \varepsilon_{n',\mathbf{k}}} \times |\langle n, \mathbf{k} | \hbar v_x | n', \mathbf{k} \rangle|^2 \delta(\hbar\omega + \varepsilon_{n,\mathbf{k}} - \varepsilon_{n',\mathbf{k}}), \quad (11.69)$$

where $\varepsilon_{n,\mathbf{k}}$ and $|n, \mathbf{k}\rangle$ are eigenvalues and eigenvectors of the Hamiltonian matrix H , $f_{n,\mathbf{k}}$ is a Fermi occupation factor and $v_a = \partial H / \hbar \partial k_a$ is the velocity operator.

Fig. 11.14 shows the optical conductivity for all the normal tetralayer graphene stacks. The rhombohedral ABCA stacking yields a $J = 4$ low-energy chiral doublet and three two-site-chain split-off bands. The optical conductivity has a divergent infrared (IR) feature associated with the $J = 4$ chiral doublet to two-site chain transitions. The onset of this absorption band has an extremum at finite $ka \approx 0.1$, implying a divergent joint density of states. Bernal ABAB stacking yields two $J = 2$ chiral doublets and four-site-chain split-off bands. The optical conductivity shows two jump-discontinuity IR features associated with $\mathbf{k} = 0$ transitions between the $J = 2$ doublets and the split-off bands. Intermediate ABCB and ABAC stackings, which are related by inversion symmetry, yield $J = 1$ and $J = 3$ chiral doublets and both two and three-site-chain split-off bands. The optical conductivity shows strong IR features associated with transitions between the chiral doublets and split-off bands. As shown in this example, the optical conductivity spectrum can provide a convenient qualitative characterization of multilayer graphene stacks [28].

11.5.3 Electrical conductivity

We can apply the multilayer graphene theory developed so far to the transport properties of multilayer graphene. (See Chapter 12 for transport theory in graphene.) From the Einstein relation, the electrical conductivity is given by

$$\sigma = e^2 \mathcal{D}(\varepsilon_F) D \quad (11.70)$$

where $\mathcal{D}(\varepsilon_F)$ is the density of states at the Fermi energy ε_F and D is the diffusion constant. In graphene, $\mathcal{D}(\varepsilon_F) = g_s g_v \rho(\varepsilon_F)$ where $g_s = 2$ and $g_v = 2$ are spin and valley degeneracy factors, respectively, and $\rho(\varepsilon_F)$ is the density

of states per spin and valley. In 2D electron system, the diffusion constant is given by $D = \frac{1}{2}v_F^2\tau_F$ where v_F is the Fermi velocity and τ_F is the relaxation time.

For simplicity, assume rotational symmetry in the energy spectrum. Then v_F and $\rho(\varepsilon_F)$ are given by

$$v_F = \frac{1}{\hbar} \left. \frac{d\varepsilon}{dk} \right|_{\varepsilon=\varepsilon_F} \quad (11.71)$$

and

$$\rho(\varepsilon_F) = \frac{k_F}{2\pi |d\varepsilon/dk|_{\varepsilon=\varepsilon_F}} = \frac{k_F}{2\pi\hbar v_F}. \quad (11.72)$$

From Fermi's golden rule, τ_F is given by

$$\frac{1}{\tau_F} = \frac{2\pi}{\hbar} n_I V_I^2 \rho(\varepsilon_F) \quad (11.73)$$

where V_I^2 is the squared effective impurity potential averaged over the azimuthal angle ϕ . In a graphene system, V_I^2 is given by

$$V_I^2 = \frac{1}{2\pi} \int_0^{2\pi} d\phi |V_I(\phi)|^2 F(\phi) (1 - \cos \phi) \quad (11.74)$$

where $V_I(\phi)$ is the matrix element of the impurity potential at ϕ and $F(\phi)$ is the chiral factor at the same band defined by

$$F(\phi) = |\langle k, \phi = 0 | k, \phi \rangle|^2. \quad (11.75)$$

Note that the relaxation time is a weighted average of the collision probability in which forward scattering ($\phi = 0$) receives very little weight.

As an example, consider simple short range scatterers neglecting interband scattering. The short range interaction can be characterized by the effective scattering cross-section length d_{sc} as

$$V_I(\phi) = \frac{2\pi e^2 d_{sc}}{\epsilon}, \quad (11.76)$$

where ϵ is the effective dielectric constant. Note that it is straightforward to extend the transport properties of multilayer graphene to other types of scatterers such as Coulomb interactions by changing the potential type in Eq. 11.74.

First, let's consider the general dependence of electrical conductivity σ on the density n for a J -chiral system. From Eq. 11.70,

$$\sigma \sim \rho(\varepsilon_F) v_F^2 \tau_F. \quad (11.77)$$

Note that $v_F \sim k_F^{J-1}$, $\tau_F^{-1} \sim n_I V_I^2 \rho(\varepsilon_F)$, $\rho(\varepsilon_F) \sim k_F/v_F \sim k_F^{2-J}$ and $n = k_F^2/\pi$. From Eq. 11.76, the short range interaction has $V_I \sim \text{constant}$. Thus, for a J -chiral system with short range scatterers, σ has the following form

$$\sigma \sim \frac{n^{J-1}}{n_I}. \quad (11.78)$$

From the chiral decomposition of multilayer graphene, arbitrarily stacked multilayer graphene is described by direct products of a set of chiral systems. Thus at low energies, or equivalently at low densities, the electrical conductivity is described by the sum of each chirality contribution.

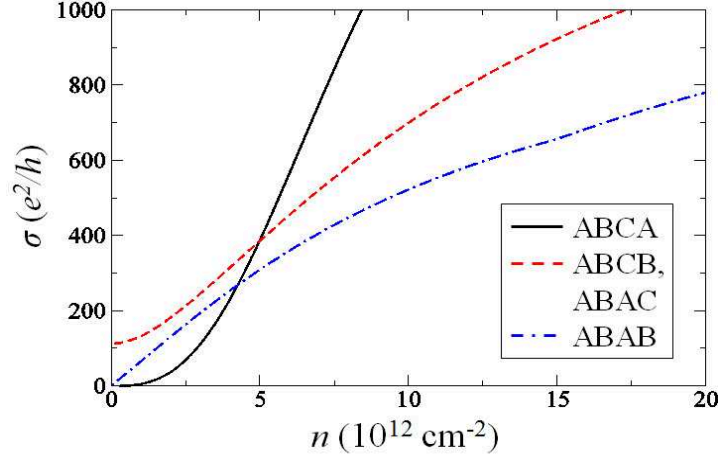


Fig. 11.15. Electrical conductivity of all the normal tetralayer graphene stacks for short range interaction with $\alpha_{gr} = e^2/(\epsilon\hbar v) = 1$ neglecting the effect of electron-hole puddles and interband scattering. The impurity density and effective impurity distance were set as $n_I = 10^{12} \text{ cm}^{-2}$ and $d_{sc} = 0.3 \text{ nm}$. For the hopping terms, $t = 3 \text{ eV}$ and $t_{\perp} = 0.1t$ were used, and other terms were neglected.

Fig. 11.15 shows the electrical conductivity of all the normal tetralayer graphene for short range interaction neglecting the effect of electron-hole puddles and interband scattering. (See [32] for discussion of the electron-hole puddles, interband scattering and other types of scatterers.) At low densities, from Eq. 11.78, ABCA stacking, which yields a $J = 4$ chiral doublet, shows n^3 density dependence, while ABAB stacking, which yields two $J = 2$ chiral doublets, shows linear density dependence in the electrical conductivity for short range interaction. Intermediate ABCB and ABAC stackings, which yield $J = 1$ and $J = 3$ chiral doublets, show the density dependence for the superposition of n^0 and n^2 . At high densities, however, energy band structure looks like a collection of monolayer graphene, thus the electrical conductivity eventually scales approximately as that of monolayer graphene.

11.6 Conclusions

We have demonstrated how the Hamiltonian of multilayer graphene is constructed using a π -orbital continuum model in the absence and presence of a magnetic field. A low-energy effective theory is derived using degenerate state perturbation theory. The low-energy bands of normal multilayer graphene can be decomposed into N_D pseudospin doublets with chirality J_i for i th doublet. Though N_D depends on the stacking sequence, $\sum_{i=1}^{N_D} J_i = N$ is always satisfied in a normal N -layer graphene stack. Many physical properties of multilayer graphene systems can be understood easily from this chiral decomposition analysis.

Acknowledgements

The work has been supported in part by the NIST-CNST/UMD-NanoCenter Cooperative Agreement. The authors thank J. J. McClelland, M. D. Stiles, S. Adam and B.R. Sahu for their valuable comments.

References

1. A. K. Geim and K. S. Novoselov, *Nature Materials* **6**, 183 (2007).
2. Andrey K. Geim and Allan H. MacDonald, *Phys. Today* **60** (8), 35 (2007).
3. Mikhail I. Katsnelson, *Mater. Today* **10**, 20 (2007).
4. A. H. Castro Neto, F. Guinea, N. M. R. Peres, K. S. Novoselov, and A. K. Geim, *Rev. Mod. Phys.* **81**, 109 (2009).
5. N. M. R. Peres, *Rev. Mod. Phys.* **82**, 2673 (2010).
6. S. Das Sarma, S. Adam, E. H. Hwang. and E. Rossi, arXiv:1003.4731 (*Rev. Mod. Phys.*, in press).
7. K. S. Novoselov, A. K. Geim, S. V. Morozov, D. Jiang, Y. Zhang, S. V. Dubonos, I. V. Grigorieva, and A. A. Firsov, *Science* **306**, 666 (2004).
8. Claire Berger, Zhimin Song, Tianbo Li, Xuebin Li, Asmerom Y. Ogbazghi, Rui Feng, Zhenting Dai, Alexei N. Marchenkov, Edward H. Conrad, Phillip N. First, and Walt A. de Heer, *J. Phys. Chem. B* **108**, 19912 (2004).
9. Taisuke Ohta, Aaron Bostwick, Thomas Seyller, Karsten Horn, and Eli Rotenberg, *Science* **313**, 951 (2006).
10. A. Rycerz, J. Tworzydł and C. W. J. Beenakker, *Nature Phys.* **3**, 172 (2007).
11. Vadim V. Cheianov, Vladimir Fal'ko, and B. L. Altshuler, *Science* **315**, 1252 (2007).
12. K. S. Novoselov, A. K. Geim, S.V. Morozov, D. Jiang, M. I. Katsnelson, I. V. Grigorieva, S. V. Dubonos, and A. A. Firsov, *Nature* **438**, 197 (2005).
13. Yuanbo Zhang, Yan-Wen Tan, Horst L. Stormer, and Philip Kim, *Nature* **438**, 201 (2005).
14. S. Latil and L. Henrard, *Phys. Rev. Lett.* **97**, 036803 (2006).
15. F. Guinea, A. H. Castro Neto, and N. M. R. Peres, *Phys. Rev. B* **73**, 245426 (2006).

16. B. Partoens and F. M. Peeters, Phys. Rev. B **74**, 075404 (2006).
17. B. Partoens and F. M. Peeters, Phys. Rev. B **75**, 193402 (2007).
18. Mikito Koshino and Tsuneya Ando, Phys. Rev. B **76**, 085425 (2007).
19. Mikito Koshino and Tsuneya Ando, Phys. Rev. B **77**, 115313 (2008).
20. Hongki Min and A. H. MacDonald, Phys. Rev. B **77**, 155416 (2008).
21. Hongki Min and A. H. MacDonald, Prog. Theor. Phys. Suppl. **176**, 227 (2008).
22. M. Aoki and H. Amawashi, Solid State Commun. **142**, 123 (2007).
23. Fan Zhang, Bhagawan Sahu, Hongki Min, and A. H. MacDonald, Phys. Rev. B **82**, 035409 (2010).
24. Kin Fai Mak, Jie Shan, and Tony F. Heinz, Phys. Rev. Lett. **104**, 176404 (2010).
25. C. L. Lu, C. P. Chang, Y. C. Huang, R. B. Chen, and M. L. Lin, Phys. Rev. B **73**, 144427 (2006).
26. Chi-Lang Lu, Hong-Chang Lin, Chi-Chuan Hwang, Jei Wang, Min-Fa Lin, and Cheng-Peng Chang, Appl. Phys. Lett. **89**, 221910 (2006).
27. Mikito Koshino and Tsuneya Ando, Solid State Commun. **149**, 1123 (2009).
28. Hongki Min and A. H. MacDonald, Phys. Rev. Lett. **103**, 067402 (2009).
29. Johan Nilsson, A. H. Neto, F. Guinea, and N. M. Peres, Phys. Rev. Lett. **97**, 266801 (2006).
30. Johan Nilsson and A. H. Castro Neto, Phys. Rev. Lett. **98**, 126801 (2007).
31. Johan Nilsson, A. H. Castro Neto, F. Guinea, and N. M. R. Peres, Phys. Rev. B **78**, 045405 (2008).
32. Hongki Min, Parakh Jain, Shaffique Adam, and M. D. Stiles, Phys. Rev. B **83**, 195117 (2011).
33. Hongki Min, E. H. Hwang, and S. Das Sarma, Phys. Rev. B **83**, 161404(R) (2011).
34. J. M. B. Lopes dos Santos, N. M. R. Peres, and A. H. Castro Neto, Phys. Rev. Lett. **99**, 256802 (2007).
35. J. Hass, F. Varchon, J. E. Millán-Otoya, M. Sprinkle, N. Sharma, W. A. de Heer, C. Berger, P. N. First, L. Magaud, and E. H. Conrad, Phys. Rev. Lett. **100**, 125504 (2008).
36. E. J. Mele, Phys. Rev. B **81**, 161405(R) (2010).
37. See for example, Paul D. Ritger and Nicholas J. Rose, *Equations with Applications* (McGraw-Hill Book Company, New York, 1968).
38. R. Saito and G. Dresselhaus and M. S. Dresselhaus, *Physical Properties of Carbon Nanotubes* (Imperial College Press, London, 1998).
39. Edward McCann and Vladimir I. Falko, Phys. Rev. Lett. **96**, 086805 (2006).
40. J. C. Charlier, J. P. Michenaud, and X. Gonze, Phys. Rev. B **46**, 4531 (1992).
41. J. J. Sakurai, *Modern Quantum Mechanics* (Addison Wesley, Reading, 1994).
42. R. R. Nair, P. Blake, A. N. Grigorenko, K. S. Novoselov, T. J. Booth, T. Stauber, N. M. R. Peres, and A. K. Geim, Science, **320**, 1308 (2008).
43. Feng Wang, Yuanbo Zhang, Chuanshan Tian, Caglar Girit, Alex Zettl, Michael Crommie, and Y. Ron Shen, Science **320**, 206 (2008).
44. Z. Q. Li, E. A. Henriksen, Z. Jiang, Z. Hao, M. C. Martin, P. Kim, H. L. Stormer, and D. N. Basov, Nature Physics **4**, 532 (2008).
45. Kin Fai Mak, Matthew Y. Sfeir, Yang Wu, Chun Hung Lui, James A. Misewich, and Tony F. Heinz, Phys. Rev. Lett. **101**, 196405 (2008).
46. P. E. Gaskell, C. Rodenchuk, H. S. Skulason, and T. Szkope, Appl. Phys. Lett. **94**, 143101 (2009).